Microphysiologically Engineered Vessel-Tumor Model to Investigate Vascular Transport Dynamics of Immune Cells

Yuwen Zhao, Yue Wu, Khayrul Islam, Ratul Paul, Yuyuan Zhou, Xiaochen Qin, Qiying Li, and Yaling Liu*

Cite This: ACS Appl. Mater. Interfaces 2024, 16, 22839−22849

Read Online

ACCESS | Metrics & More | Article Recommendations | Supporting Information

ABSTRACT: Cancer immunotherapy has emerged as a promising therapeutic strategy to combat cancer effectively. However, it is hard to observe and quantify how this in vivo process happens. Three-dimensional (3D) microfluidic vessel-tumor models offer valuable capability to study how immune cells transport during cancer progression. We presented an advanced 3D vessel-supported tumor model consisting of the endothelial lumen and vessel network for the study of T cells' transportation. The process of T cell transport through the vessel network and interaction with tumor spheroids was represented and monitored in vitro. Specifically, we demonstrate that the endothelial glycocalyx serving in the T cells' transport can influence the endothelium-immune interaction. Furthermore, after vascular transport, how programmed cell death protein 1 (PD-1) immune checkpoint inhibition influences the delivered activated-T cells on tumor killing was evaluated. Our in vitro vessel-tumor model provides a microphysiologically engineered platform to represent T cell vascular transportation during tumor immunotherapy. The reported innovative vessel-tumor platform is believed to have the potential to explore the tumor-induced immune response mechanism and preclinically evaluate immunotherapy's effectiveness.
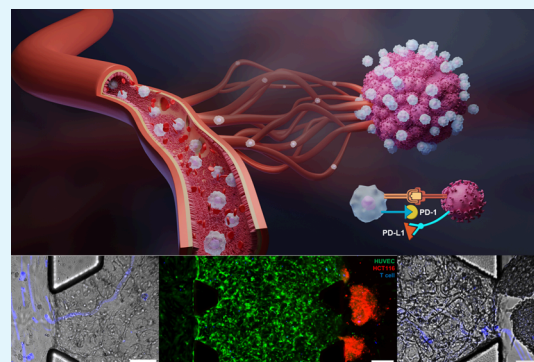
KEYWORDS: microfluidics, cancer immunotherapy, vascular transport, tumor microphysiology, vessel-tumor-on-chip

1. INTRODUCTION

Cancer remains one of the leading causes of death worldwide. As per data from the American Cancer Society, more than 600,000 individuals lost their lives to cancer in the United States in 2022.[1] Cancer immunotherapy is a promising therapeutic approach that effectively treats primary and metastatic neoplastic lesions. Immunotherapy has demonstrated clinical efficacy by harnessing the immune system's power to eliminate cancer cells. It has significantly advanced the field of immune-oncology research, resulting in better outcomes for patients.[2,3] Immunotherapies are generally classified into different categories, which involve the transplantation of engineered antitumor immune cells, such as chimeric antigen receptor (CAR)-T cells and CAR-natural killer (NK) cells, the use of immune checkpoint inhibitors (ICIs, for example, anti-PD-1 antibodies, and anticytotoxic T-lymphocyte-associated protein 4 or anti-CTLA-4 antibodies), the administration of cytokines like interleukins and interferons, and the utilization of therapeutic vaccines.[4−7] Accordingly, immune checkpoint inhibition in immunotherapy has drastically altered clinical outcomes for cancer patients with lasting clinical benefits, including cures in some patients.[7] The diverse responses of patients to ICIs emphasize the need to develop swift and efficient means to evaluate their effectiveness.[8,9] To succeed in

these endeavors, improved preclinical models are necessary to inform immunotherapy in vasculature tumor studies.[10]

Traditional immunotherapy delivery relies heavily on vascular transport. The vascular system is a natural mechanism in the immune response that heavily depends on its proper functioning.[11−14] It enables immune cells and signaling molecules to move through the blood vessels and reach sites of cancerous cell occurrence or injury, facilitating an effective immune response. Furthermore, the efficiency of immune therapy is influenced by the internal vessel network, which exhibits significant diversity between healthy and tumor tissues and the impact on immune cell recruitment.[15−17] The endothelial cell surface is typically coated with a layer of polysaccharides, which serves as the interface between the blood and the endothelium.[18−20] The endothelial glycocalyx (VGCX) influences the immune cell behavior during vascular transport, and the inherent features of VGCX are evident from experimental and computational models.[21−25] Since most
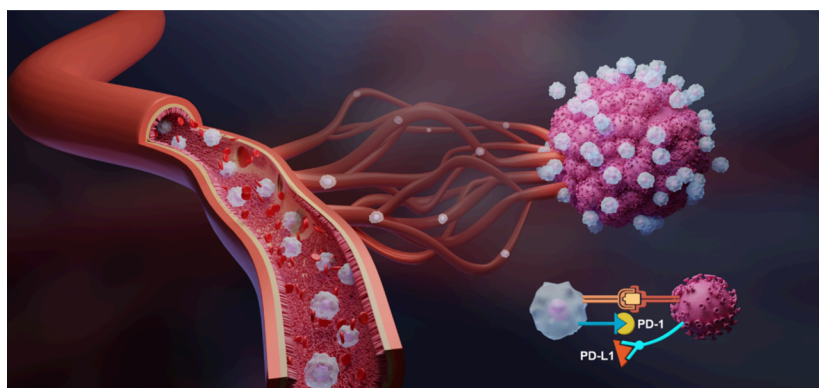
Figure 1. Illustration of the T cell vascular transportation in tumor immunotherapy that involves three main components—blood vessel, tumor, and transporting T cells.

leukocyte adhesion receptors (cell adhesion molecules, CAMs) are located in postcapillary venules, such as intercellular adhesion molecule (ICAM), endothelial-leukocyte adhesion molecule (E-Selectin), and P-Selectin, shedding of the venular glycocalyx may play an important role during the immune response.[18,26−33] Thus, the ability to model the structure and transport function of blood vessels in a comprehensive setting is important for understanding the physiological processes of immunotherapy.[34,35]

The microfluidic technique offers a flexible approach to engineer tumor-on-chip platforms and recreates vascular transport in vitro.[36−41] Several studies focus on the early stage of vascularization and manipulate different strategies to promote the growth of endothelial cells around the tumor by altering the microphysiological environment.[42−51] Dey et al. explored the cytotoxicity induced by CAR-T in the breast tumor microenvironment based on blood vessels and dynamic flow.[52] Similarly, Ayuso et al. used a microfluidic model to simulate and study NK cell migration, cytotoxicity, and antibody-dependent cytotoxicity in complex 3D structures.[15] Wan et al. reported a new strategy based on their existing tumor vascularization platform. They improved the vascularization by sequentially adding fibroblasts to form tumor spheres, verifying the ability to enhance drug delivery, cell trafficking, and CAR-T cell response.[51] Due to the highly complex process of vascular transport under tumor immunotherapy in vivo, representing the interaction between tumor, vessel, and immune cells in vitro is essential.[14,53−55] Meanwhile, the application of ICIs as a critical factor in the therapeutic assessment of vascular−tumor−immune cell interactions in such an immune process remains underexplored. Inspired by these novel approaches, we developed a method to visualize the immune therapy process and investigate the physiology of this interaction, which reflects the human body.

Our study devised a perfusable vascular network, facilitating the creation of a vessel-tumor model to induce the T cells' transportation. The concept is illustrated in Figure 1. This model closely mimics the intermediate structure that transports T cells from the main blood vessels to the outflow toward the tumor.[56] Subsequently, we conducted assessments on T cell cytotoxicity, particularly focusing on the PD-1/PD-L1 immune checkpoint blockage. A significant decrease in tumor viability was observed after T cell stimulation and immune checkpoint inhibition. These findings demonstrate an in vitro vessel-tumor model that helps to understand the progression of

immune vascular transportation and overcomes microphysiological transport limits.

2. MATERIALS AND METHODS

2.1. Microfluidic Device Design and Fabrication. Based on the platform mentioned in our previous study, the vessel-generation microfluidic device (VGMFD) design using AutoCAD software was fabricated with standard soft lithography techniques using negative photoresist SU-8 2150 (Kayaku Advanced Materials).[57] The fabrication was finished at the Institute for Functional Materials and Devices (I-FMD), Integrated Nanofabrication and Cleanroom Facility (INCF) at Lehigh University. Polydimethylsiloxane (PDMS) (SYLGARD 184, Dow Corning Corporation) was used for the replica of the SU-8 master mold, and the PDMS was cured at 80 °C for 1 h and then peeled off for bonding with glass slides. The device was designed to be 350 μm in height, and a 200 μm distance was considered between the microposts to provide sufficient surface tension. Four loading reservoirs and two gel loading inlets were punched into the PDMS layer by 4 and 1 mm biopsy punches (World Precision Instruments), respectively. All the devices were presterilized by autoclave before the experiments.

2.2. Cell Culture and Reagents. Human umbilical vein endothelial primary cells (HUVECs) and human colorectal carcinoma cell lines (HCT116) were purchased from Lonza and the American Type Culture Collection (ATCC), respectively. HUVECs were cultured in EBM-2 Basal Medium (Lonza), supplied with Microvascular Endothelial Cell Growth Medium SingleQuots supplements (EGM-2 MV, Lonza) and 1% Antibiotic-Antimycotic (Gibco). HUVECs from passages 3−8 were used in the experiments. The HCT116 were cultured in Dulbecco's modified eagle medium (DMEM, Gibco), supplied with 10% fetal bovine serum (FBS, Gibco) and 1% penicillin-streptomycin (Bio-Techne Corporation). The T cells were obtained from the Human Immunology Core of Penn Medicine and maintained in RPMI-1640 (ATCC), supplied with 10% FBS, 1% Pen-Strep, and 10 ng/mL Recombinant Human IL-2 (Biolegend). All of the cells were maintained regularly with medium change each other day. For HUVECs and HCT116, 0.05% Trypsin-EDTA (Bio-Techne Corp.) was employed for the passaging.

2.3. Endothelium Layer and Vessel-Tumor Formation and Culture. The vessel networks were created using a seeding method with a concentration of 8 × 10^6/mL HUVECs. The HUVECs were seeded in a fibrin gel composed of bovine fibrinogen and thrombin (Sigma-Aldrich). After the gel was prepared, it was injected into the gel-laden channel and allowed to cure for 20 min. Following the curing process, hydraulic pressure was applied to induce interstitial flow, facilitating the vessel network's formation. On the third day, the medium channels of the device were coated with a 0.2% gelatin solution for 1 h. Subsequently, HUVECs were seeded onto gelatin-coated channels. The device was tilted to ensure uniform coverage of the endothelium layer, and fresh HUVECs were introduced every half

an hour, ensuring that all channels' sides were coated with the endothelial layer.

The tumor spheroids were generated by commercial AggreWell Microwell Plates (STEMCELL Technologies). In brief, the microwells were precoated with an antiadherence-rinsing solution (STEMCELL Technologies). HCT116 cells were harvested and seeded into the microwells at 1.2×10^5 cells/mL. After 3 days of culture, tumor spheroids with a desired size of approximately 150 μm were formed. Subsequently, the tumor spheroids were transferred to the medium channel of the VGMFD, which did not contain an endothelium layer. The tumor spheroids adhered to the outlet of the vessel network, creating a vessel-tumor model. Before the tumor spheroids were transferred into the microfluidic device, HUVECs and tumor spheroids were stained with CellTracker Green CMFDA and CellTracker Red CMTPX Dye (Invitrogen), respectively.

2.4. Endothelium Glycocalyx Degradation and T Cell Adhesion. The processes mentioned in our previous paper follow the VGCX layer degradation.[58] The Neuraminidase enzyme (Neur) was used for one of the main components of the degradation of endothelium glycocalyx, sialic acid, a glycocalyx component of immune system regulatory relevance.[59] Wheat germ agglutinin (WGA) lectin was considered to characterize the glycocalyx layer. The T cells were then perfused through the endothelial layer to evaluate T cell adhesion. The T cells were prepared at 3×10^5 cells/mL, with a flow rate of 10 μL/min, and this flow rate mimicked the wall shear stress inside the vessel.

2.5. Computational Simulation. We have crafted a coarse-grained molecular dynamics model to elucidate the influence of VGCX on ligand−receptor binding between T cells and the endothelial monolayer. This model employs the Cooke−Deserno membrane representation technique, a renowned approach for simulating interactions between ligands and receptors.[60] Our model adopts a dual-layered approach for the T cell using a Cooke−Deserno three-bead membrane representation. Each lipid in this representation is portrayed as a trio of discrete beads. These beads symbolize the hydrophilic headgroup and the two hydrophobic tail groups (as illustrated in blue in Figure 4A). This configuration adeptly encapsulates the amphiphilic nature of the lipids. The coarse-grained beads are interconnected through a finite extensible nonlinear elastic bond, which ensures the preservation of the inherent character of the lipids. To further enhance the realism of our model, a harmonic angular potential is incorporated to maintain the beads' straightened configuration. By adjusting the Lennard-Jones parameters, we fine-tuned the affinity between the ligand and receptor to mirror the experimentally observed adhesion rates between ligand receptors. To represent the ligand within our model, we employed a ligand chain composed of six beads. This chain is strategically affixed to the outer head layer of the T cell membrane. To emulate natural variability, our model ensures that the ligand chain is attached to ∼20% of the randomly selected sites on the outer head layer of the T cell membrane. This method not only introduces randomness but also captures the inherent heterogeneity observed in biological membranes.

In our model, to capture the essence of VGCX, we have adopted a six-bead chain representation. Each bead in this chain is designed to symbolize a segment or a functional unit of the VGCX components. This coarse-grained approach simplifies the intricate molecular details of VGCX while retaining its essential features, making it computationally feasible to study its interactions and dynamics. A fundamental aspect of our representation is the designed lack of affinity of these beads toward the T cell ligand achieved through tuning parameters of Lennard-Jones potential. In the biological context, VGCX can act as a barrier or a mediator for various cellular interactions. By ensuring that our simulated beads exhibit no affinity for the T cell ligand, we are emphasizing the role of the VGCX as a distinct and semipermeable entity. This design choice ensures that any interactions or lack thereof between the VGCX and the T cell ligand in our simulations are not due to inherent attractions but are a result of the broader system dynamics and conditions. This distinction is vital for accurately

deciphering the role of VGCX in ligand−receptor interactions and understanding its influence on cellular processes.

The interaction affinities between the ligand (on T cells) and the receptors are defined using the Lennard-Jones potential, a time-honored approach in molecular dynamics simulations. The Lennard-Jones potential describes the potential energy between two particles based on their distance, encapsulating both their attractive and repulsive interactions. By meticulously adjusting the parameters of this potential, we can modulate the strength and nature of interactions between the ligand and receptors. This provides a platform for a comprehensive and nuanced exploration of their binding dynamics, illuminating factors that govern the specificity, duration, and strength of these pivotal biological interactions. The membrane representation and the associated parameters were described in our previous publication.[61]

2.6. T Cell Stimulation and Immune Checkpoint Blockage. A concentration of 1 μg/mL of antihuman CD3 and 2 μg/mL of antihuman CD28 antibodies (Biolegend) was added to the culture medium to activate the T cells. The cells were then incubated for at least 48 h to allow for activation before conducting the experiments. For the PD-1/PD-L1 immune checkpoint inhibition, cells were treated with a concentration of 50 nM PD-1/PD-L1 inhibitor 3 (IB3, Selleck Chemicals). The inhibitor was added to the culture medium, and the cells were incubated with the inhibitor overnight concurrently with the experiments.

2.7. Immunocytochemistry. Samples were labeled using immunocytochemistry techniques to characterize the vessel network, and PD-L1 in tumors was used to identify specific proteins. Samples were washed in 1×PBS (Gibco) three times and then fixed with 4% paraformaldehyde (PFA, Thermo Fisher Scientific) for 30 min. Then, following 0.1% Triton X-100 permeabilization for 15 min to prevent nonspecific bind, 3% bovine serum albumin (BSA, Sigma-Aldrich) was used for the blocking for 1 h. The vessel networks were labeled with platelet endothelial cell adhesion molecules by PE/Cyanine 5 antihuman CD31 (Biolegend) and F-actin by Phalloidin-FITC (Abcam). The tumor spheroids, epithelial cell adhesion molecule, and PD-L1 were stained with Alexa 488 antihuman EpCAM and Alexa 594 antihuman PD-L1 (Biolegend), respectively. The nucleus was counterstained with DAPI (Invitrogen).

2.8. T Cell Cytotoxicity and Infiltration Evaluation. After the vessel-tumor model was created, T cells under four conditions were introduced: inactivated T cells without PD-1/PD-L1 inhibition, inactivated T cells with PD-1/PD-L1 inhibition, activated T cells without PD-1/PD-L1 inhibition, and activated T cells with PD-1/PD-L1 inhibition. The ratio of the target cells to the effective cells was 1:10 (in which the T cells were the effector cells, and the tumor cells served as the target cells) and started from the T cells surrounding the tumor spheroids; T cells and tumor spheroids were cocultured for 24 h. For the T cell cytotoxicity evaluation, the vessel-tumor model was first washed with medium twice, and then live/dead staining solution, which was prepared in medium with a concentration of 5 and 10 μM Calcein AM (Corning) and propidium iodide (PI, Biotium), respectively, was used and incubated for 30 min at 37 °C before imaging. For the T cell infiltration evaluation, the T cells and tumor spheroids were stained with CellTracker Blue CMAC (Invitrogen) and CellTracker Green CMFDA Dye, respectively. After coculture, confocal images were captured under the same focal plane to visualize the interaction between T cells and tumor spheroids. The distances that T cells invaded toward the center of the tumor spheroids were measured to assess the infiltration efficiency. To analyze the images and categorize different regions within the tumor spheroids by contour lines, a gap of 10 μm was indicated between each line.

2.9. Imaging and Statistical Analysis. The images were captured by using either an Olympus IX70 inverted microscope or a Nikon C2+ laser scanning confocal microscope. Data collection and imaging analysis were conducted using the NIH ImageJ software. The images were captured in the same field of view with background subtraction for all quantified data, including the glycocalyx condition, viability test, and infiltration. The normalized T cell adhesion rate is given as

$$\text{Adhesion rate (\%)} = \frac{N_{\text{ad}}}{N_{\text{total}}} \times 100\%$$

where N_{ad} is the number of the attached T cells on the endothelial layer after the perfusion, and N_{total} is the average number of the T cells that have been perfused per frame per ROI.

Spheroid viability was calculated based on the ratio of the spheroid's area of green fluorescence through the maximum intensity projection images. At least five images were analyzed for each experimental condition to ensure accuracy. The experiments were repeated at least three times, and quantification was performed on over 50 cells or 10 spheroids in each group. Statistical analysis was carried out using an independent, two-tailed student t test, with a p-value of less than 0.05 considered statistically significant.

3. RESULT AND DISCUSSION

3.1. Vessel-Tumor On-Chip Model Generation. We developed an in vitro vessel-tumor model using a three-channel VGMFD. This model aimed to replicate the structural characteristics of the vascularized tumor microenvironment, as demonstrated in Figure 2. The device consisted of three
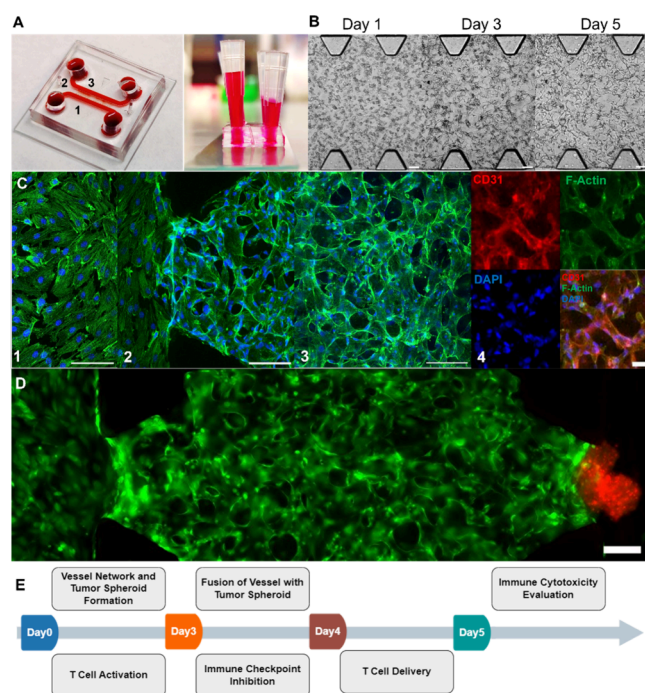
Figure 2. Setup of the vessel-tumor on a chip model. (A) PDMS-based vessel-generation microfluidic device. (B) Time course of vasculature self-organization. Scale bar: 100 μm. (C) Confocal images of the endothelial cell monolayer and the vessel network. Red, green, and blue represent CD31, F-actin, and nucleus staining, respectively. (1−3): Monolayer of the vessel lumen, endothelial cells at the anastomosis, and vessel network. Scale bar: 100 μm. (4) Characterization of the vessel network. Scale bar: 25 μm. (D) Full fluorescent view of the vessel-supported tumor model. Green and red indicate HUVECs and HCT116, respectively. Scale bar: 100 μm. (E) Schematic diagram showing the experimental design of immune dynamic investigation on the vessel-tumor model.

distinct regions: the endothelial lumen region, the vessel network region, and the tumor spheroid region. The VGMFD had two gel-loading inlets, with the center channel (channel 2) containing microposts to prevent gel leakage (Figure 2A). This channel facilitated vasculogenesis and allowed for perfusion of the vasculature. Channels 1 and 3 were designated explicitly for

the flow of the medium. Channel 1 generated the endothelial cell monolayer, while channel 3 served as the region for housing the tumor spheroids. To serve as reservoirs for the medium, 200 μL micropipette tips were inserted at the inlets of channels 1 and 3. The medium flow was initially introduced from channel 3, creating hydraulic pressure and interstitial flow that facilitated the diffusion of the medium through the hydrogel present in channel 2. This process supported the formation of a perfusable vessel network, typically around day 5 of culture (Figure 2B,C). By day 3 of the vasculature self-assembly process, preformed HCT116 tumor spheroids were introduced into channel 3 of the microfluidic device. The tilting of the device allowed for the tumor spheroids to adhere to the outlet of the vessel network, resulting in a seamless fusion between the tumor spheroids and the hydrogel (Figures 2D and S1). This integration created a close interaction between the tumor spheroids and the vascular network, simulating the tumor microenvironment and facilitating the study of tumor progression and therapeutic responses within this in vitro model. The size of the tumor spheroids used in our model was intentionally selected to load into anastomosis region through the gaps between the microposts in the VGMFD. This enabled the efficient delivery of cells and therapeutic agents to the tumor spheroids, mimicking the transport dynamics observed in the vascularized tumor microenvironment.

**3.2. Endothelium Glycocalyx Status Influences T Cell Adhesion.** Being the first structure on the endothelium to interact with the bloodstream and circulating cells, VGCX encompasses an array of adhesion receptors including integrins, immunoglobulins, and selectins. When the system interacts with blood flow under varying conditions, the corresponding feedback influences the adhesion of T cells to blood vessels, which is mediated by receptors and regulates the physiological response of T cells during tumor immunotherapy. Thus, we employed an enzymatic method to examine the influence of VGCX degradation on the mechanical interactions between T cells and the endothelial monolayer to mimic the tumor-mediated VGCX function. Our approach focused on the degradation of sialic acid residues in VGCX using Neur, a sialidase enzyme. By targeting the sialic acid components, we aimed to assess the effects of VGCX degradation on the mechanical dynamics of T cell−endothelial cell interactions within the system. By treating the endothelial monolayer with Neur for 1 h, we could degrade the VGCX effectively (Figure 3A). The degradation of VGCX led to noticeable changes in its characteristics. Specifically, we observed a significant decrease in the average thickness of the glycocalyx after 60 min of treatment (Figure 3B). The treated glycocalyx exhibited a thickness of approximately 3.3 times thinner compared to the nontreated glycocalyx. Additionally, we observed a substantial reduction in the coverage area of VGCX, with a decrease of 63.1% after the same duration of treatment (Figure 3C). These findings demonstrate the effective removal and modification of the VGCX through Neur treatment. The enzymatic degradation of the glycocalyx led to the direct exposure of the cell membrane to the surrounding microenvironment, eliminating the protective barrier provided by the VGCX. This exposure allowed for closer interactions between T cells and endothelial cells, potentially altering their mechanical interactions.

We introduced T cells into the system to mimic the transportation of T cells through the endothelial cell monolayer. The T cells were prepared at a concentration of
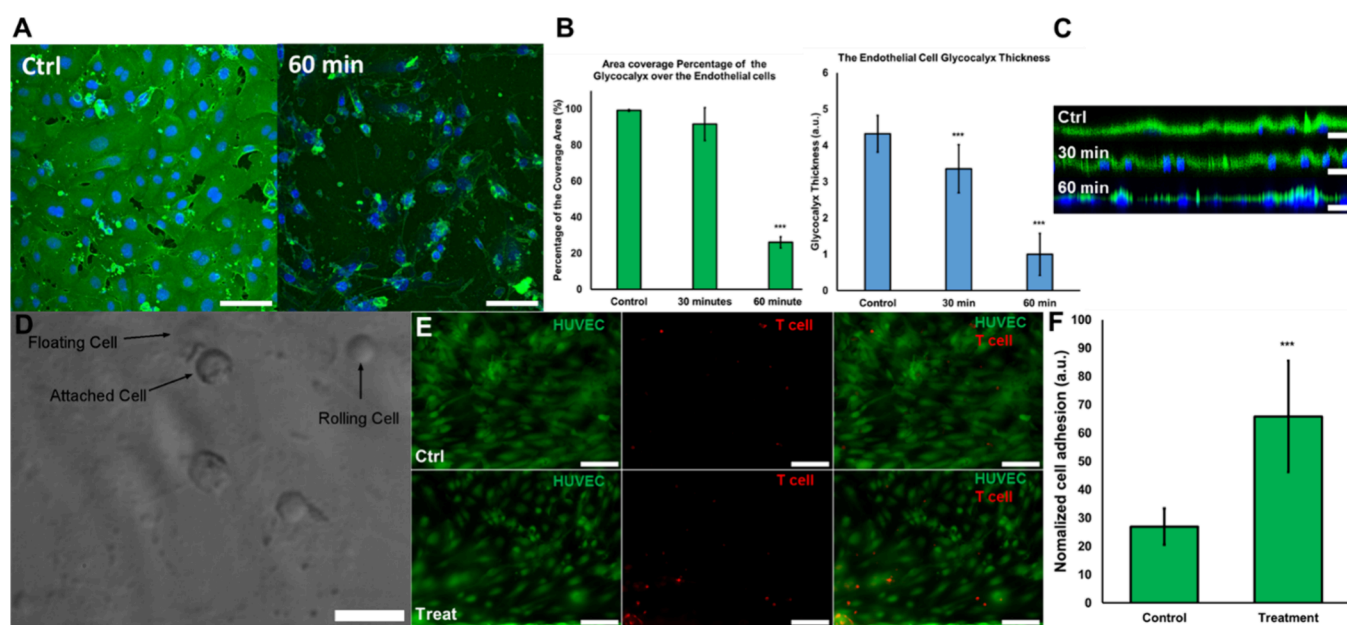
Figure 3. Endothelium glycocalyx conditions after enzymatic degradation. (A) Neur enzyme-treated endothelium glycocalyx component sialic acid for 0 min (control) and 60 min. The sialic acid was stained green, and the nucleus was stained blue. Scale bar: 50 μm. (B) Quantified characterization of the glycocalyx layer coverage area and thickness before and after Neur treatment at different times. (C) Confocal scan of the endothelium glycocalyx was degraded by the enzyme over time. Green: sialic acid; blue: nucleus. Scale bar: 25 μm. (D, E) Images of T cell adhesion to the nontreated endothelium layer (control group) and 60 min-treated endothelium layer (treatment group). The HUVECs were stained with CellTracker Green CMFDA, and T cells were stained with CellTracker Red CMTPX. Scale bar: 25 μm. (F) Statistical analysis of the normalized rate of T cells adhesion to the endothelium layer. Data representing over 100 cells in each group are expressed as mean $\pm$ S.E.M. (***$p < 0.001$, **$p < 0.01$, *$p < 0.05$).
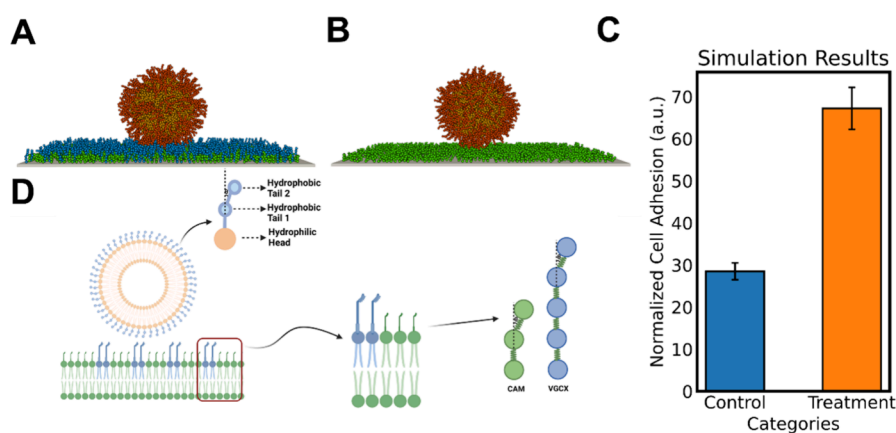

Figure 4. Visualization of ligand−receptor binding simulations. (A) Interaction of T cell ligand and CAM receptor in the presence of VGCX, (B) and in the absence of VGCX. (C) Comparison of normalized cell adhesion between the treatment group (lacking VGCX) and the control group (with VGCX). (D) Schematic depiction of the simulation algorithm, where VGCX is denoted by 6 coarse-grained beads and AMCAM is denoted by 3 beads. The schematic is generated through Biorender.

3×10^5 cells/mL and were introduced into the flow at a rate of 10 μL/min. This flow rate was chosen to provide a similar wall shear stress (WSS) observed in the venous vessel, typically around 1 dyn/cm². By subjecting the T cells to this flow condition, we aimed to recreate the physiological environment and study their ability to transmigrate across the endothelial cell monolayer (Video S1). The WSS does not lead to substantial removal of the VGCX. Conversely, following enzyme treatment, T cells exhibit three distinct states, floating, rolling, and attached, mimicking their movement within the bloodstream (Figure 3D). Additionally, our findings revealed that after 60 min of VGCX degradation, T cells had increased adhesion to the endothelial lumen. This provides evidence of

the T cell interaction with endothelial cells within the microenvironment. Comparing the rate of T cell adhesion to that of the endothelial monolayer, a noticeable increase in the number of attached T cells was observed in association with VGCX degradation. In the absence of the sialic acid layer, there was an observed increase of over 2.4 times in the conglutination of T cells to HUVECs (Figure 3E,F). As a result, with increased adherence, less amount of T cells enters the vessel inlet, which alters the transport behavior.

A molecular dynamics computational model is also developed to undersee this process. In the simulation, the interaction between the T cell ligand and its corresponding receptor is depicted in Figure 4. Delving deeper into the
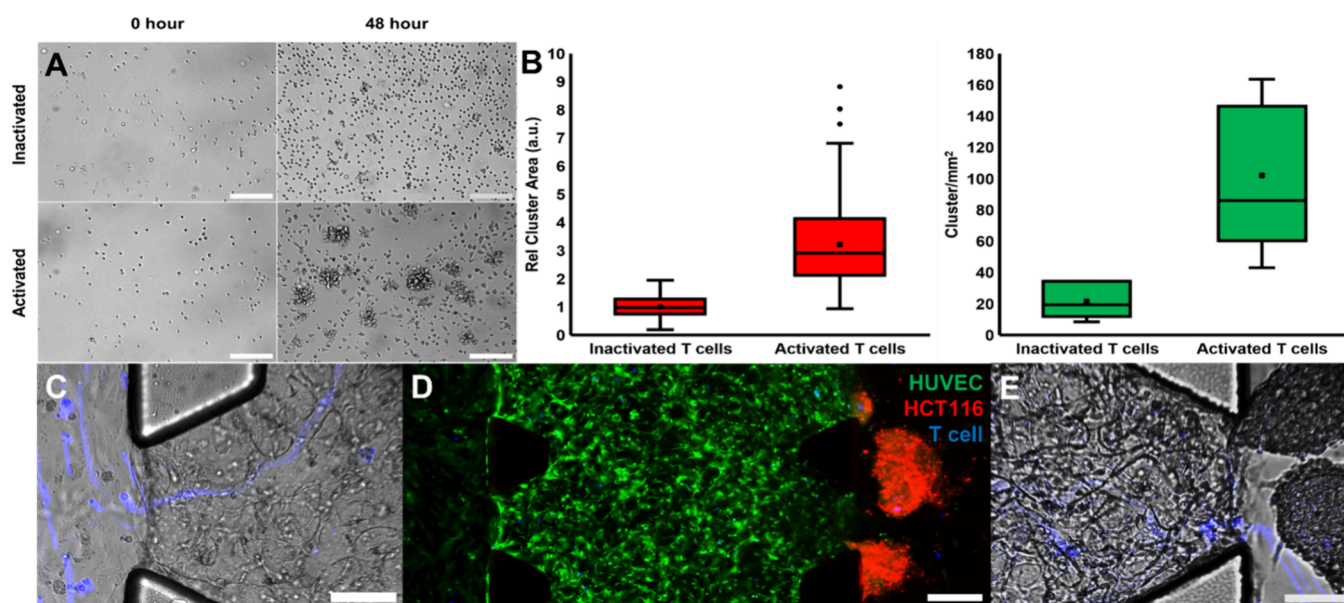
Figure 5. T cell activation and T cells interact with endothelial cells and tumor spheroids. (A) Anti-CD3 and anti-CD28 stimulated T cells after 48 h. Scale bar: 100 μm. (B) Relative cluster size and cluster number under the field of view between the inactivated T cells and activated T cells. (C) Trajectory of the T cell was denoted in blue, indicating the movement from the endothelial layer to the vessel network. Scale bar: 50 μm. (D) T cell introduction into the vessel-supported tumor model. With the purfusable vessel network, the T cells appeared in the HUVECs vessel network and surrounded the tumor spheroids. The HUVECs, HCT116 tumor spheroids, and T cells were stained with CellTracker green CMFDA, red CMTPX, and blue CMAC, respectively. Scale bar: 200 μm. (E) Trajectory of the T cell was denoted in blue, indicating the movement from the vessel network toward the tumor spheroid. Scale bar: 50 μm.

specifics, Figure 4A illustrates the presence of VGCX, a dense, anionic, and carbohydrate-rich layer covering the cell surface. Notably, when the VGCX is present, there is a marked reduction in the adhesion between the T cell ligand and receptor. This suggests that the VGCX may play a role in modulating this interaction, possibly acting as a barrier or mediator. On the other hand, Figure 4B provides a contrasting view, showcasing the interaction between the T cell ligand and receptor in the absence of the VGCX. The difference in adhesion levels between the two scenarios is further quantified in a bar chart (Figure 4C), which presents the normalized adhesion values for both the control group (with VGCX) and the treatment group (without VGCX). Outcomes from the simulations align closely with the experimental results. The scheme of the simulations is shown in Figure 4D.

3.3. Perfusable Network Allows for T Cell Transport toward the Tumor Spheroids. The typical immune response requires T cell activation. T cells have the potential to infiltrate the tumor environment after the stimulation. Thus, comparing the inactivated and activated T cells being stimulated at the antigen recognition site and the tumor microenvironment is important. In general, by implementing the surface antigens of antigen-presenting cells (APCs), the CD3-receptor and CD28 coreceptor are able to reprogram the T cells. Upon stimulation, the T lymphocytes start to proliferate and elicit a pathogen-specific immune response.[62] Some notable phenomena were counted for demonstrating the T cell activation, commonly with clustering and deformation.[63,64] To assess the efficacy of the anti-CD3 and anti-CD28 treatment, we examined bright field images taken within 48 h of the initiation of the treatment (Figure 5A,B). We analyzed the aggregated clusters based on the size of each cluster and the number of clusters present within the field of view. In contrast, the inactivated T cells demonstrate a lower propensity to form clusters, while a higher occurrence of T cell clusters is observed on the surface of antigen receptors (anti-CD3 and anti-CD28), as expected. The analysis reveals that the clusters formed by activated T cells exhibit an average size approximately 3.3 times larger than those created by nonactivated T cells. Furthermore, upon analyzing the number of clusters within the field of view, it was observed that an average of 102 clusters formed in a 1-millimeter square area after 48 h of stimulation, with a maximum of 164 clusters. In comparison, only 21 clusters were generated without stimulation, accounting for only 21% compared to the presence of anti-CD3 and anti-CD28 supplements. These findings strongly indicate that successful activation was achieved in accordance with the expected nature of stimulated T cells.

Our next step is cooperating with all of the setups and allowing the purfusable vessel network (Figure 5C) to transport the T cells. Once the hydrogel and tumor spheroids fused together (with the tumor spheroids attaching and growing into the hydrogel, Video S2), the T cells were introduced into the vessel network. The bottom port of the inlet was blocked to enforce the T cells entering the vessel networks. After a flow period of five min, we could observe the presence of transported T cells surrounding the tumor spheroids (Figure 5D) and the transported T cells perfusion in the vessels. Furthermore, by stacking up the dynamical locations of T cells, the T cells' transportation was able to be recorded by Ximea XiB CB 120-CM Camera and traced from the video through ImageJ processing by z-stack standard deviation (Figures S1 and S2; Videos S3 and S4). The trajectory represented the path of the T cell movement in the vessel network and how the T cell was transported toward the tumor spheroid (Figure 5E). Accordingly, the vessel-tumor model that we developed enabled the tumor to adhere to the
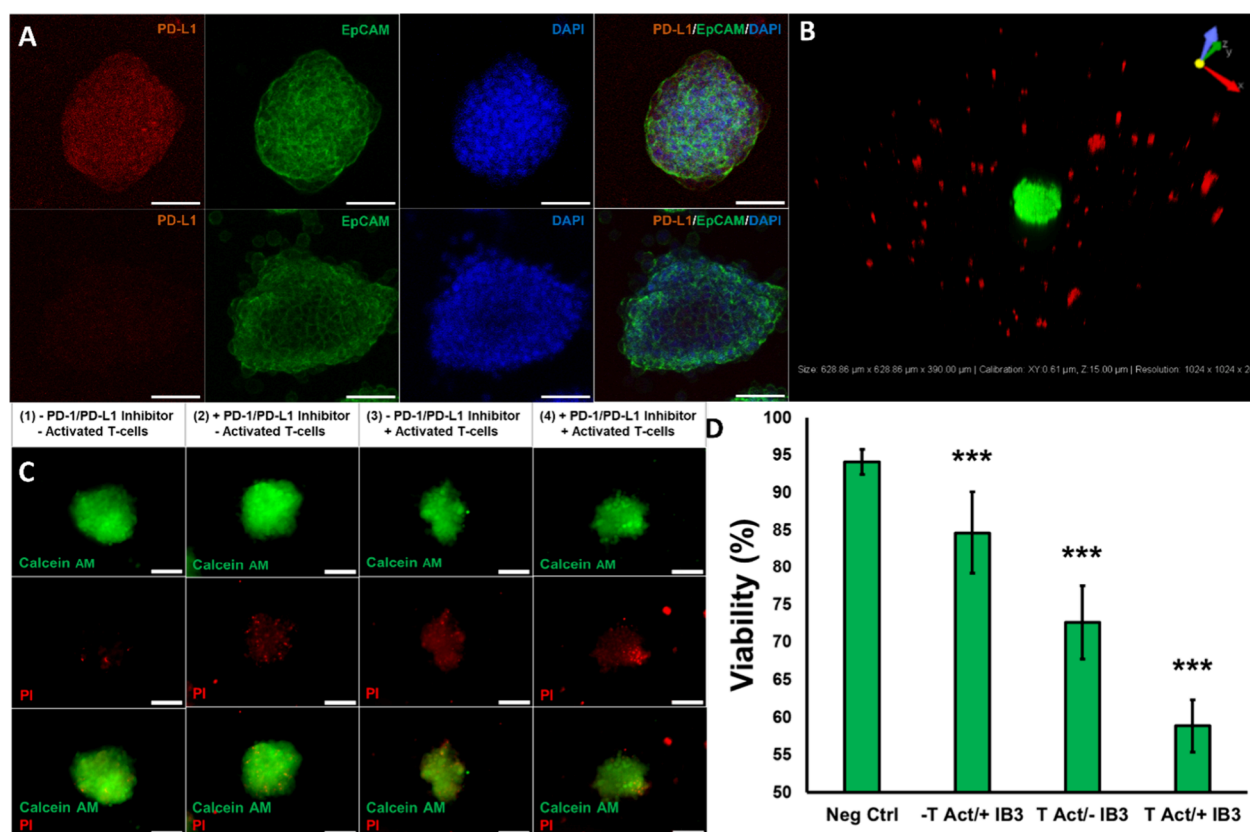
Figure 6. Tumor spheroid immune checkpoint blockage and T cell cytotoxicity evaluation. (A) Immunofluorescent images of tumor spheroids with and without PD-L1 inhibitor treatment. Orange: PD-L1; Green: EpCAM; Blue: nucleus. (B) Three-dimensional confocal scan of tumor spheroid after T cell appearance inside the channel. Green: tumor spheroid; Red: T cells. (C) T cell cytotoxicity to the tumor spheroid under conditions: (1) without PD-1/PD-L1 inhibition and inactivated T cells, (2) with PD-1/PD-L1 inhibition and inactivated T cells, (3) without PD-1/PD-L1 inhibition and activated T cells, and (4) with PD-1/PD-L1 inhibition and activated T cells. The tumor spheroids viability was validated by the live/dead staining, where the living cells were stained in green by Calcein AM and dead cells stained in red by PI. (D) Statistical tumor spheroid viability under different conditions. Data representing over 30 spheroids in each group are expressed as mean ± S.E.M. (***$p < 0.001$, **$p < 0.01$, *$p < 0.05$). Scale bar: 100 μm.

outlets of the vessel network. The tumor's proximity to the vessels enhances the interaction between T cells and tumor cells, potentially impacting the immune response and tumor microenvironment dynamics.

3.4. Inhibition of Immune Checkpoints Promotes the Immune Response in the Vessel-Tumor Model. As an FDA-approved cancer treatment strategy, targeting immune checkpoint PD-1/PD-L1 is a significant immunotherapy approach. Herein, we examined the impact of immune checkpoint inhibition on both tumor cells and T cells and assessed the efficacy of immunotherapy in T cells. To determine the expression of PD-L1 in our tumor spheroids, we first stained the HCT116 tumor with anti-PD-L1 before and after the PD-1/PD-L1 inhibitor process. It has been presented that HCT116 internally has PD-L1 expression, suppressing the T cell interaction with the tumor. After overnight treatment, the inhibition driven from the IB3 downgraded the PD-L1 signals, allowing the T cells to be more sensitive and capable of targeting the tumor spheroids (Figure 6A). Meanwhile, upon stimulation, the PD-1 level expressed in the T cells increased as the stimulation time passed. Thus, the 48 h-activated T cells brought a PD-1 expression over 50% of the whole T cell population (Figure S3), which showed its potential as PD-1/PD-L1 immune checkpoint inhibition treatment.

Then, we validated the cytotoxicity of the activated T cells combined with the blockage of PD-1/PD-L1, which is considered a traditional immunotherapy treatment. As previously mentioned, while the T cells appeared around the tumor spheroids (Figure 6B), we started 24 h of coculture to evaluate the tumor viability by the immune therapy process. Four conditions have been incorporated, consisting of negative control, the groups with either T cell activation or PD-1/PD-L1 inhibition, or groups containing both T cell activation and IB3 treatment. Following the stimulation, we observed that the activated T cells displayed enhanced cytotoxicity against tumor spheroids. A 3.6-fold increase in cytotoxicity occurs compared to the groups without T cell activation, and the tumor viability in the T cell activation-only group is 84.6%. Furthermore, when we utilized a PD-1/PD-L1 inhibitor, we observed a significant reduction in tumor viability even without T cell activation, and it reached levels 1.6 times lower than those of the control groups, as shown in Figure 6C,D. We combined T cell activation and immune checkpoint blockade, notably reducing tumor viability to below 60%, which is 35% lower than the negative control.

3.5. Infiltration of the Delivered T Cells Present in the Tumor. The dynamic process of T cell infiltration was characterized by using confocal scanning (Figure 7). As the infiltration time increases, the delivered T cells were observed
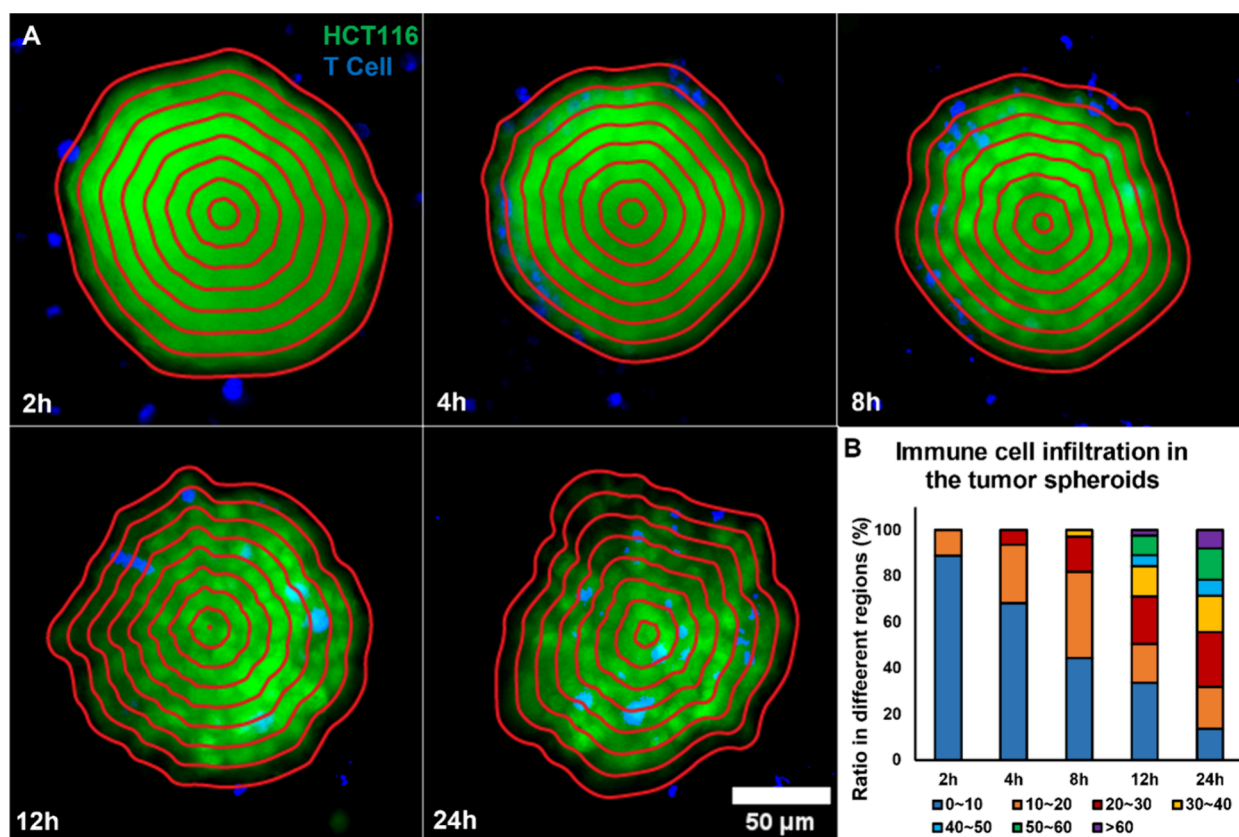
Figure 7. Confocal scan of T cell infiltration in the tumor spheroids after T cells perfused through the vessel network. (A) Delivered T cells invaded under different time courses, from 2 to 24 h. The distance was classified with gradient contour lines, and each line stands for a 10 μm gap. Green: Tumor spheroid, blue: T cell; red: gradient contour line. All of the images were derived from z-stack maximum intensity projection. Scale bar: 50 μm. (B) T cell distribution ratio plot in the tumor spheroids and $n = 3$ for each time point.

to penetrate deep into the tumor spheroids, reaching the center (the infiltration distance exceeding 60 μm). To visualize the process, we employed contour lines to delineate distinct regions based on the distance from the edge to the center of each tumor spheroid. With the average size of tumor spheroids being 150 μm, we set the length between each contour line to 10 μm, ensuring that each tumor spheroid was divided into eight independent regions. We counted the invaded distance, considering any distance beyond 60 μm as the center of the tumor. Only 11% of the T cells (T cells colocalizing with the tumor spheroid divided by the number of all T cells in the field of view) began to infiltrate the tumor during the initial 2 h, shown as orange in Figure 7B. However, after 24 h, over 90% of the T cells were present in the spheroids. Notably, the most efficient infiltration occurred between 2 and 4 h, following the introduction of T cells. After a 12 h period, we could observe the presence of T cells in the center of the tumors. This finding indicates that, in our model, the immune activity primarily initiates and becomes noticeable within the first 12 h.

Solid tumors are highly related to the vessel-dominated microphysiological environment, significantly influencing transportation efficiency in in vivo immune therapy.[65,66] The understanding of vessel—tumor—immune cell interactions has been particularly obscure. To address the challenge, it is necessary to understand the vascular transport process by an in vitro strategy. Thus, generating a visualizable vessel-tumor model becomes crucial, particularly in studying tumor—immune interactions.[51,67]

In this study, we developed a microphysiologically engineered vessel-tumor model to evaluate immune cell vascular transport and immunotherapy efficiency. By involving different compositions in the microfluidic platform, our new model is capable of representing the process of T cell transportation through various vessel-tumor compositions. Moreover, the on-chip tumor model enables the assessment of the T cell-killing behavior after vascular delivery, which provides real-time monitoring of the interaction of vessels, tumors, and T cells.

Specifically, we investigated the effect of VGCX on endothelial cells, which influences T cell adhesion. The removal of sialic acid from the endothelial lumen led to an increased adhesion of T cells to the endothelial layer. Subsequently, we observed the tumor—immune cell interactions as the T cells successfully transported through the vessel to the tumor spheroids. Finally, we examined the immune checkpoint inhibition on the platform and evaluated the effectiveness of immunotherapy on delivered T cells. It was found that PD-1 immune checkpoint inhibition of the delivered T cells results in higher cytotoxicity and reduced tumor viability. Generally, the vessel-tumor model demonstrated the potential to monitor T cell vascular transport and assess immunotherapy effectiveness.

4. CONCLUSIONS

In summary, we developed an in vitro vessel-tumor model featured for T cell vascular transportation, which mimics the interactions between the tumor, endothelial, and immune cells

in vivo. By utilizing the platform, we reconstituted a 3D vascular network as the intermediate section between the blood vessel and solid tumor, allowing T cells to transport through the network and monitor the proceeding. The cytotoxicity of the T cells has been evaluated, and the delivered T cells have shown a proper tumor-killing function (less than a third compared with the group without the ICIs). Together, these results represent the progress of vascular transport during tumor immunotherapy. Furthermore, the platform may pave the way for studying tumor treatment outcomes with the combined therapy of immunotherapy and chemotherapy.

◼ ASSOCIATED CONTENT

Ⓢ Supporting Information

The Supporting Information is available free of charge at https://pubs.acs.org/doi/10.1021/acsami.4c00391.

> Detailed experimental methods (PDF)
>
> Confocal scan of the vessel-tumor model, T cell entering and exiting the vessel network, and 4 T cell dynamic after VGCX degradation (AVI)

◼ AUTHOR INFORMATION

Corresponding Author

Yaling Liu − *Department of Bioengineering and Department of Mechanical Engineering and Mechanics, Lehigh University, Bethlehem, Pennsylvania 18015, United States;* ⓞ orcid.org/0000-0002-4519-3358; Email: yal310@lehigh.edu

Authors

Yuwen Zhao − *Department of Bioengineering, Lehigh University, Bethlehem, Pennsylvania 18015, United States;* ⓞ orcid.org/0000-0001-5020-9134

Yue Wu − *Department of Bioengineering, Lehigh University, Bethlehem, Pennsylvania 18015, United States;* ⓞ orcid.org/0000-0002-6564-2093

Khayrul Islam − *Department of Mechanical Engineering and Mechanics, Lehigh University, Bethlehem, Pennsylvania 18015, United States*

Ratul Paul − *Department of Mechanical Engineering and Mechanics, Lehigh University, Bethlehem, Pennsylvania 18015, United States*

Yuyuan Zhou − *Department of Bioengineering, Lehigh University, Bethlehem, Pennsylvania 18015, United States;* ⓞ orcid.org/0000-0002-8317-4115

Xiaochen Qin − *Department of Bioengineering, Lehigh University, Bethlehem, Pennsylvania 18015, United States;* ⓞ orcid.org/0000-0003-0051-2500

Qiying Li − *Department of Electrical and Computer Engineering, Lehigh University, Bethlehem, Pennsylvania 18015, United States*

Complete contact information is available at:
https://pubs.acs.org/10.1021/acsami.4c00391

Author Contributions

Y.L. conceived and supervised the study. Y.Z., Y.W., and Y.L. designed and performed the experiments. Y.Z. and Y.Z. collected and analyzed the data. R.P. and Q.L. assisted with data analysis. K.I. assisted with the simulation. Y.Z. wrote the manuscript. Y.W., Y.Z., K.I., X.Q., and Y.L. revised the manuscript. All authors discussed the results and approved the submission.

Notes

The authors declare no competing financial interest.

◼ ACKNOWLEDGMENTS

◼ REFERENCES

(1) Siegel, R. L.; Miller, K. D.; Fuchs, H. E.; Jemal, A. Cancer Statistics, 2022. *CA Cancer J. Clin.* **2022**, *72* (1), 7−33.

(2) Shelton, S. E.; Nguyen, H. T.; Barbie, D. A.; Kamm, R. D. Engineering Approaches for Studying Immune-Tumor Cell Interactions and Immunotherapy. *iScience* **2021**, *24* (1), No. 101985.

(3) Lee, J. H.; Shao, S.; Kim, M.; Fernandes, S. M.; Brown, J. R.; Kam, L. C. Multi-Factor Clustering Incorporating Cell Motility Predicts T Cell Expansion Potential. *Front Cell Dev Biol.* **2021**, *9*, No. 648925.

(4) Eggermont, L. J.; Paulis, L. E.; Tel, J.; Figdor, C. G. Towards Efficient Cancer Immunotherapy: Advances in Developing Artificial Antigen-Presenting Cells. *Trends Biotechnol.* **2014**, *32* (9), 456−465.

(5) June, C. H. Adoptive T Cell Therapy for Cancer in the Clinic. *J. Clin. Invest.* **2007**, *117* (6), 1466−1476.

(6) Paul, S.; Lal, G. The Molecular Mechanism of Natural Killer Cells Function and Its Importance in Cancer Immunotherapy. *Front. Immunol.* **2017**, *8*, 1124.

(7) Sharma, P.; Goswami, S.; Raychaudhuri, D.; Siddiqui, B. A.; Singh, P.; Nagarajan, A.; Liu, J.; Subudhi, S. K.; Poon, C.; Gant, K. L.; Herbrich, S. M.; Anandhan, S.; Islam, S.; Amit, M.; Anandappa, G.; Allison, J. P. Immune Checkpoint Therapy-Current Perspectives and Future Directions. *Cell* **2023**, *186* (8), 1652−1669.

(8) Wei, S. C.; Anang, N.-A. A. S.; Sharma, R.; Andrews, M. C.; Reuben, A.; Levine, J. H.; Cogdill, A. P.; Mancuso, J. J.; Wargo, J. A.; Pe'er, D.; Allison, J. P. Combination Anti-CTLA-4 plus Anti-PD-1 Checkpoint Blockade Utilizes Cellular Mechanisms Partially Distinct from Monotherapies. *Proc. Natl. Acad. Sci. U. S. A.* **2019**, *116* (45), 22699−22709.

(9) Munn, L. L.; Jain, R. K. Vascular Regulation of Antitumor Immunity. *Science* **2019**, *365* (6453), 544−545.

(10) Lamplugh, Z.; Fan, Y. Vascular Microenvironment, Tumor Immunity and Immunotherapy. *Front. Immunol.* **2021**, *12*, No. 811485.

(11) Ehlers, H.; Nicolas, A.; Schavemaker, F.; Heijmans, J. P. M.; Bulst, M.; Trietsch, S. J.; van den Broek, L. J. Vascular Inflammation on a Chip: A Scalable Platform for Trans-Endothelial Electrical Resistance and Immune Cell Migration. *Front. Immunol.* **2023**, *14*, No. 1118624.

(12) Beard, D. A.; Bassingthwaighte, J. B. Advection and Diffusion of Substances in Biological Tissues with Complex Vascular Networks. *Ann. Biomed. Eng.* **2000**, *28* (3), 253−268.

(13) Weyand, C. M.; Goronzy, J. J. Immune Mechanisms in Medium and Large-Vessel Vasculitis. *Nat. Rev. Rheumatol.* **2013**, *9* (12), 731−740.

(14) Wu, Y.; Zhou, Y.; Qin, X.; Liu, Y. From Cell Spheroids to Vascularized Cancer Organoids: Microfluidic Tumor-on-a-Chip Models for Preclinical Drug Evaluations. *Biomicrofluidics* **2021**, *15* (6), No. 061503.

(15) Ayuso, J. M.; Truttschel, R.; Gong, M. M.; Humayun, M.; Virumbrales-Munoz, M.; Vitek, R.; Felder, M.; Gillies, S. D.; Sondel, P.; Wisinski, K. B.; Patankar, M.; Beebe, D. J.; Skala, M. C. Evaluating Natural Killer Cell Cytotoxicity against Solid Tumors Using a Microfluidic Model. *Oncoimmunology* **2019**, *8* (3), No. 1553477.

(16) Shin, J. H.; Jeong, J.; Maher, S. E.; Lee, H.-W.; Lim, J.; Bothwell, A. L. M. Colon Cancer Cells Acquire Immune Regulatory Molecules from Tumor-Infiltrating Lymphocytes by Trogocytosis. *Proc. Natl. Acad. Sci. U. S. A.* **2021**, *118* (48), No. e2110241118.

(17) Schaaf, M. B.; Garg, A. D.; Agostinis, P. Defining the Role of the Tumor Vasculature in Antitumor Immunity and Immunotherapy. *Cell Death Dis.* **2018**, *9* (2), 115.

(18) Lipowsky, H. H. The Endothelial Glycocalyx as a Barrier to Leukocyte Adhesion and Its Mediation by Extracellular Proteases. *Ann. Biomed. Eng.* **2012**, *40* (4), 840−848.

(19) Mitchell, M. J.; King, M. R. Physical Biology in Cancer. 3. The Role of Cell Glycocalyx in Vascular Transport of Circulating Tumor Cells. *Am. J. Physiol. Cell Physiol.* **2014**, *306* (2), C89−97.

(20) Sperandio, M.; Gleissner, C. A.; Ley, K. Glycosylation in Immune Cell Trafficking. *Immunol. Rev.* **2009**, *230* (1), 97−113.

(21) Weinbaum, S.; Tarbell, J. M.; Damiano, E. R. The Structure and Function of the Endothelial Glycocalyx Layer. *Annu. Rev. Biomed. Eng.* **2007**, *9*, 121−167.

(22) Jiang, X. Z.; Luo, K. H.; Ventikos, Y. Understanding the Role of Endothelial Glycocalyx in Mechanotransduction via Computational Simulation: A Mini Review. *Front Cell Dev Biol.* **2021**, *9*, No. 732815.

(23) Banerjee, T.; Gosai, A.; Yousefi, N.; Garibay, O. O.; Seal, S.; Balasubramanian, G. Examining Sialic Acid Derivatives as Potential Inhibitors of SARS-CoV-2 Spike Protein Receptor Binding Domain. *J. Biomol. Struct. Dyn.* **2023**, 1−17.

(24) Yousefi, N.; Yazdani-Jahromi, M.; Tayebi, A.; Kolanthai, E.; Neal, C. J.; Banerjee, T.; Gosai, A.; Balasubramanian, G.; Seal, S.; Ozmen Garibay, O. Binding Site-Augmented DTA: Enabling a next-Generation Pipeline for Interpretable Prediction Models in Drug Repurposing. *Brief. Bioinform.* **2023**, *24* (3), No. bbad136.

(25) Villalba, N.; Baby, S.; Yuan, S. Y. The Endothelial Glycocalyx as a Double-Edged Sword in Microvascular Homeostasis and Pathogenesis. *Front Cell Dev Biol.* **2021**, *9*, No. 711003.

(26) Iigo, Y.; Suematsu, M.; Higashida, T.; Oheda, J.; Matsumoto, K.; Wakabayashi, Y.; Ishimura, Y.; Miyasaka, M.; Takashi, T. Constitutive Expression of ICAM-1 in Rat Microvascular Systems Analyzed by Laser Confocal Microscopy. *Am. J. Physiol.* **1997**, *273* (1 Pt 2), H138−H147.

(27) Hu, Z.; Cano, I.; D'Amore, P. A. Update on the Role of the Endothelial Glycocalyx in Angiogenesis and Vascular Inflammation. *Front Cell Dev Biol.* **2021**, *9*, No. 734276.

(28) Zhao, Y.; Chien, S.; Weinbaum, S. Dynamic Contact Forces on Leukocyte Microvilli and Their Penetration of the Endothelial Glycocalyx. *Biophys. J.* **2001**, *80* (3), 1124−1140.

(29) Li, Q.; Shao, S.; Zhu, Z.; Chen, J.; Hao, J.; Bai, Y.; Li, B.; Dang, E.; Wang, G. An IGFBP7hi Endothelial Cell Subset Drives T Cell Extravasation in Psoriasis via Endothelial Glycocalyx Degradation. *J. Clin. Invest.* **2023**, *133* (9), No. e160451.

(30) Zhao, Y.; Richardson, K.; Yang, R.; Bousraou, Z.; Lee, Y. K.; Fasciano, S.; Wang, S. Notch Signaling and Fluid Shear Stress in Regulating Osteogenic Differentiation. *Frontiers in Bioengineering and Biotechnology* **2022**, *10*, No. 1007430.

(31) Reitsma, S.; Slaaf, D. W.; Vink, H.; van Zandvoort, M. A. M. J.; oude Egbrink, M. G. A. The Endothelial Glycocalyx: Composition, Functions, and Visualization. *Pflugers Arch.* **2007**, *454* (3), 345−359.

(32) Mulivor, A. W.; Lipowsky, H. H. Role of Glycocalyx in Leukocyte-Endothelial Cell Adhesion. *Am. J. Physiol. Heart Circ. Physiol.* **2002**, *283* (4), H1282−H1291.

(33) Zahr, A.; Alcaide, P.; Yang, J.; Jones, A.; Gregory, M.; de la Paz, N. G.; Patel-Hett, S.; Nevers, T.; Koirala, A.; Luscinskas, F. W.; Saint-Geniez, M.; Ksander, B.; D'Amore, P. A.; Argüeso, P. Endomucin Prevents Leukocyte-Endothelial Cell Adhesion and Has a Critical Role under Resting and Inflammatory Conditions. *Nat. Commun.* **2016**, *7*, No. 10363.

(34) Paek, J.; Park, S. E.; Lu, Q.; Park, K.-T.; Cho, M.; Oh, J. M.; Kwon, K. W.; Yi, Y.-S.; Song, J. W.; Edelstein, H. I.; Ishibashi, J.; Yang, W.; Myerson, J. W.; Kiseleva, R. Y.; Aprelev, P.; Hood, E. D.; Stambolian, D.; Seale, P.; Muzykantov, V. R.; Huh, D. Microphysiological Engineering of Self-Assembled and Perfusable Microvascular Beds for the Production of Vascularized Three-Dimensional Human Microtissues. *ACS Nano* **2019**, *13* (7), 7627−7643.

(35) Li, M.; Song, X.; Jin, S.; Ye, K. 3D Tumor Model Biofabrication. *Bio-Design and Manufacturing* **2021**, *4* (3), 526−540.

(36) Parlato, S.; Grisanti, G.; Sinibaldi, G.; Peruzzi, G.; Casciola, C. M.; Gabriele, L. Tumor-on-a-Chip Platforms to Study Cancer-Immune System Crosstalk in the Era of Immunotherapy. *Lab Chip* **2021**, *21* (2), 234−253.

(37) Zhou, Y.; Wu, Y.; Paul, R.; Qin, X.; Liu, Y. Hierarchical Vessel Network-Supported Tumor Model-on-a-Chip Constructed by Induced Spontaneous Anastomosis. *ACS Appl. Mater. Interfaces* **2023**, *15* (5), 6431−6441.

(38) Miller, C. P.; Shin, W.; Ahn, E. H.; Kim, H. J.; Kim, D.-H. Engineering Microphysiological Immune System Responses on Chips. *Trends Biotechnol.* **2020**, *38* (8), 857−872.

(39) Wu, Y.; Zhao, Y.; Islam, K.; Zhou, Y.; Omidi, S.; Berdichevsky, Y.; Liu, Y. Acoustofluidic Engineering Functional Vessel-on-a-Chip. *ACS Biomater. Sci. Eng.* **2023**, *9* (11), 6273−6281.

(40) Paul, R.; Zhao, Y.; Coster, D.; Qin, X.; Islam, K.; Wu, Y.; Liu, Y. Rapid Prototyping of High-Resolution Large Format Microfluidic Device through Maskless Image Guided in-Situ Photopolymerization. *Nat. Commun.* **2023**, *14* (1), 4520.

(41) Chen, B.; Wu, Y.; Ao, Z.; Cai, H.; Nunez, A.; Liu, Y.; Foley, J.; Nephew, K.; Lu, X.; Guo, F. High-Throughput Acoustofluidic Fabrication of Tumor Spheroids. *Lab Chip* **2019**, *19* (10), 1755−1763.

(42) Dura, B.; Servos, M. M.; Barry, R. M.; Ploegh, H. L.; Dougan, S. K.; Voldman, J. Longitudinal Multiparameter Assay of Lymphocyte Interactions from Onset by Microfluidic Cell Pairing and Culture. *Proc. Natl. Acad. Sci. U. S. A.* **2016**, *113* (26), E3599−E3608.

(43) Zhao, Y.; Yu, X.; Li, J. Manipulation of Immune−vascular Crosstalk: New Strategies towards Cancer Treatment. *Acta Pharm. Sin B* **2020**, *10* (11), 2018−2036.

(44) Song, J.; Choi, H.; Koh, S. K.; Park, D.; Yu, J.; Kang, H.; Kim, Y.; Cho, D.; Jeon, N. L. High-Throughput 3D In Vitro Tumor Vasculature Model for Real-Time Monitoring of Immune Cell Infiltration and Cytotoxicity. *Front. Immunol.* **2021**, *12*, No. 733317.

(45) Siemann, D. W. The Unique Characteristics of Tumor Vasculature and Preclinical Evidence for Its Selective Disruption by Tumor-Vascular Disrupting Agents. *Cancer Treat. Rev.* **2011**, *37* (1), 63−74.

(46) Xiao, W.; Ruan, S.; Yu, W.; Wang, R.; Hu, C.; Liu, R.; Gao, H. Normalizing Tumor Vessels To Increase the Enzyme-Induced Retention and Targeting of Gold Nanoparticle for Breast Cancer Imaging and Treatment. *Mol. Pharmaceutics* **2017**, *14* (10), 3489−3498.

(47) Lanitis, E.; Irving, M.; Coukos, G. Targeting the Tumor Vasculature to Enhance T Cell Activity. *Curr. Opin. Immunol.* **2015**, *33*, 55−63.

(48) Liu, Z.; Wang, Y.; Huang, Y.; Kim, B. Y. S.; Shan, H.; Wu, D.; Jiang, W. Tumor Vasculatures: A New Target for Cancer Immunotherapy. *Trends Pharmacol. Sci.* **2019**, *40* (9), 613−623.

(49) Haase, K.; Offeddu, G. S.; Gillrie, M. R.; Kamm, R. D. Endothelial Regulation of Drug Transport in a 3D Vascularized Tumor Model. *Adv. Funct. Mater.* **2020**, *30* (48), No. 2002444.

(50) Quintard, C.; Tubbs, E.; Jonsson, G.; Jiao, J.; Wang, J.; Werschler, N.; Laporte, C.; Pitaval, A.; Bah, T.-S.; Pomeranz, G.; Bissardon, C.; Kaal, J.; Leopoldi, A.; Long, D. A.; Blandin, P.; Achard, J.-L.; Battail, C.; Hagelkruys, A.; Navarro, F.; Fouillet, Y.; Penninger, J. M.; Gidrol, X. A Microfluidic Platform Integrating Functional Vascularized Organoids-on-Chip. *Nat. Commun.* **2024**, *15* (1), 1452.

(51) Wan, Z.; Floryan, M. A.; Coughlin, M. F.; Zhang, S.; Zhong, A. X.; Shelton, S. E.; Wang, X.; Xu, C.; Barbie, D. A.; Kamm, R. D. New Strategy for Promoting Vascularization in Tumor Spheroids in a Microfluidic Assay. *Adv. Healthcare Mater.* **2022**, *12*, No. e2201784.

(52) Dey, M.; Kim, M. H.; Dogan, M.; Nagamine, M.; Kozhaya, L.; Celik, N.; Unutmaz, D.; Ozbolat, I. T. Chemotherapeutics and CAR-T Cell-based Immunotherapeutics Screening on a 3D Bioprinted Vascularized Breast Tumor Model. *Adv. Funct. Mater.* **2022**, *32*, No. 2203966.

(53) Gurski, L. A.; Jha, A. K.; Zhang, C.; Jia, X.; Farach-Carson, M. C. Hyaluronic Acid-Based Hydrogels as 3D Matrices for in Vitro

Evaluation of Chemotherapeutic Drugs Using Poorly Adherent Prostate Cancer Cells. *Biomaterials* **2009**, *30* (30), 6076−6085.

(54) Zheng, Y.; Wang, S.; Xue, X.; Xu, A.; Liao, W.; Deng, A.; Dai, G.; Liu, A. P.; Fu, J. Notch Signaling in Regulating Angiogenesis in a 3D Biomimetic Environment. *Lab Chip* **2017**, *17* (11), 1948−1959.

(55) Wang, S.; Sun, J.; Xiao, Y.; Lu, Y.; Zhang, D. D.; Wong, P. K. Intercellular Tension Negatively Regulates Angiogenic Sprouting of Endothelial Tip Cells via Notch1-Dll4 Signaling. *Adv. Biosyst* **2017**, *1* (1−2), No. 1600019.

(56) Iovene, A.; Zhao, Y.; Wang, S.; Amoako, K. Bioactive Polymeric Materials for the Advancement of Regenerative Medicine. *J. Funct. Biomater.* **2021**, *12* (1), 14.

(57) Wu, Y.; Zhao, Y.; Zhou, Y.; Islam, K.; Liu, Y. Microfluidic Droplet-Assisted Fabrication of Vessel-Supported Tumors for Preclinical Drug Discovery. *ACS Appl. Mater. Interfaces* **2023**, *15* (12), 15152−15161.

(58) Wu, Y.; Zhou, Y.; Paul, R.; Qin, X.; Islam, K.; Liu, Y. Adaptable Microfluidic Vessel-on-a-Chip Platform for Investigating Tumor Metastatic Transport in Bloodstream. *Anal. Chem.* **2022**, *94* (35), 12159−12166.

(59) Möckl, L. The Emerging Role of the Mammalian Glycocalyx in Functional Membrane Organization and Immune System Regulation. *Front. Cell Dev. Biol.* **2020**, *8*, 253.

(60) Cooke, I. R.; Deserno, M. Solvent-Free Model for Self-Assembling Fluid Bilayer Membranes: Stabilization of the Fluid Phase Based on Broad Attractive Tail Potentials. *J. Chem. Phys.* **2005**, *123* (22), No. 224710.

(61) Islam, K.; Razizadeh, M.; Liu, Y. Coarse-Grained Molecular Simulation of Extracellular Vesicle Squeezing for Drug Loading. *Phys. Chem. Chem. Phys.* **2023**, *25* (17), 12308−12321.

(62) Heylmann, D.; Badura, J.; Becker, H.; Fahrer, J.; Kaina, B. Sensitivity of CD3/CD28-Stimulated versus Non-Stimulated Lymphocytes to Ionizing Radiation and Genotoxic Anticancer Drugs: Key Role of ATM in the Differential Radiation Response. *Cell Death Dis.* **2018**, *9* (11), 1053.

(63) Borger, J. G.; Morrison, V. L.; Filby, A.; Garcia, C.; Uotila, L. M.; Simbari, F.; Fagerholm, S. C.; Zamoyska, R. Caveolin-1 Influences LFA-1 Redistribution upon TCR Stimulation in CD8 T Cells. *J. Immunol.* **2017**, *199* (3), 874−884.

(64) Smith, Z. J.; Wang, J.-C. E.; Quataert, S. A.; Berger, A. J. Integrated Raman and Angular Scattering Microscopy Reveals Chemical and Morphological Differences between Activated and Nonactivated CD8+ T Lymphocytes. *J. Biomed. Opt.* **2010**, *15* (3), No. 036021.

(65) Quail, D. F.; Joyce, J. A. Microenvironmental Regulation of Tumor Progression and Metastasis. *Nat. Med.* **2013**, *19* (11), 1423−1437.

(66) Zhang, S.; Wan, Z.; Kamm, R. D. Vascularized Organoids on a Chip: Strategies for Engineering Organoids with Functional Vasculature. *Lab Chip* **2021**, *21* (3), 473−488.

(67) Anderson, K. G.; Stromnes, I. M.; Greenberg, P. D. Obstacles Posed by the Tumor Microenvironment to T Cell Activity: A Case for Synergistic Therapies. *Cancer Cell* **2017**, *31* (3), 311−325.